arXiv:1408.5940v1 [astro-ph.SR] 25 Aug 2014

The Launch Region of the SVS 13 Outflow and Jet

Klaus W. Hodapp[1], Rolf Chini[2,3]

ABSTRACT

We present the results of Keck Telescope laser adaptive optics integral field spectroscopy with OSIRIS of the innermost regions of the NGC 1333 SVS 13 outflow that forms the system of Herbig-Haro objects 7-11. We find a bright 0.″2 long microjet traced by the emission of shock-excited [FeII]. Beyond the extent of this jet, we find a series of bubbles and fragments of bubbles that are traced in the lower excitation H_2 1–0 S(1) line. While the most recent outflow activity is directed almost precisely (PA $\approx 145^\circ$) to the south-east of SVS 13, there is clear indication that prior bubble ejections were pointed in different directions. Within these variations, a clear connection of the newly observed bubble ejection events to the well-known, poorly collimated HH 7-11 system of Herbig-Haro objects is established. Astrometry of the youngest of the expanding shock fronts at 3 epochs covering a time span of over two years gives kinematic ages for two of these. The kinematic age of the youngest bubble is slightly older than the historically observed last photometric outburst of SVS 13 in 1990, consistent with that event launching the bubble and some deceleration of its expansion. A re-evaluation of historic infrared photometry and new data show that SVS 13 has not yet returned to its brightness before that outburst and thus shows a behavior similar to FUor outbursts, albeit with a smaller amplitude. We postulate that the creation of a series of bubbles and the changes in outflow direction are indicative of a precessing disk and accretion events triggered by a repetitive phenomenon possibly linked to the orbit of a close binary companion. However, our high-resolution images in the H and K bands do not directly detect any companion object. We have tried, but failed to detect, the kinematic signature of rotation of the microjet in the [FeII] emission line at 1.644 μm.

[1] Institute for Astronomy, University of Hawaii, 640 N. Aohoku Place, Hilo, HI 96720, USA
email: *hodapp@ifa.hawaii.edu*

[2] Astronomisches Institut, Ruhr-Universität Bochum, Universitätsstraße 150, D-44801 Bochum, Germany
email: *rolf.chini@astro.ruhr-uni-bochum.de*

[2] Instituto de Astronomia, Universidad Catolica del Norte, Avenida Angamos 0610, Antofagasta, Chile

Subject headings: infrared: stars — ISM: Herbig-Haro objects — ISM: jets and outflows — stars: formation — stars: individual (SVS 13) — stars: variables: other

1. INTRODUCTION

The accretion of matter onto a forming star is inextricably associated with mass outflow. This manifests itself as well-collimated jets typically observed in higher excitation shock-excited forbidden lines such as [SII] or [FeII], or lower excitation emission of shock-exited H_2. Larger-scale and older outflows are typically detected in CO emission of entrained ambient material. While the precise mechanism of jet launching is actively being debated, steady progress has been made in observational studies of the launch regions of jets. Such studies require the highest possible spatial resolutions, since all theories postulate that jets are launched from the inner regions of the protostellar disks on spatial scales of a few AU, or from the protostar's magnetosphere, on scales of a stellar diameter.

At present, the highest spatial resolutions for studies of the jet launch regions are achieved at optical wavelengths with the Hubble Space Telescope (HST), and at near-infrared wavelengths with adaptive optics on large ground-based telescopes. The near-infrared techniques have the advantage of being able to better penetrate dust extinction, so that the jet launch regions of more deeply embedded, generally younger stars can be observed. However, near-infrared laser-guide-star adaptive optics observations today are still limited by the requirement to have a fairy bright, optically visible ($R \lessapprox 16$) tip-tilt reference star close to the object, or that the object itself can serve this purpose. As a consequence, even at near-infrared wavelengths, the best candidates for high spatial resolution studies are objects near the end of their Class I phase or early in the classical T Tauri star phase because in nearby molecular (dark) clouds, the only available optical tip-tilt reference star is often the young star itself.

In this paper we present detailed adaptive-optics corrected integral field spectroscopy of NGC 1333 SVS 13, the driving source of the famous chain of Herbig-Haro objects HH 7-11 (Herbig & Jones 1983). Other commonly used names for SVS 13 are V512 Per and 2MASS J03290375+3116039. The SVS 13 outflow appears relatively poorly collimated and is comprised of a number of individual shock fronts, as can be seen in Fig. 1 that presents a progression from seeing-limited to diffraction-limited images of the SVS 13 outflow. There is an anti-parallel counter outflow visible, but it is displaced from the axis of the HH 7-11

outflow. For a general overview of NGC 1333 and a review of the literature on the SVS 13 subcluster, the reader is referred to the review article by Walawender et al. (2008). The Two Micron All Sky Survey (2MASS) position of SVS 13 is $3^h\ 29^m\ 03^s.759\ +31^\circ\ 16'\ 03''.99$ ($J2000$) at epoch 1999 Nov. 26 with an accuracy of $\pm\ 0''.10$ (Skrutskie et al. 2006). This position lies between the VLA configuration A radio position of VLA 4B at 3.6 cm reported by Anglada, Rodríguez, & Torrelles (2000) at $3^h\ 29^m\ 03^s.74\ +31^\circ\ 16'\ 04''.15$ ($J2000$) with an effective epoch of 1997.9 and estimated errors of $\pm\ 0''.05$ and the 7 mm VLA configuration B position of the same radio source, which Anglada et al. (2004) give as $3^h\ 29^m\ 03^s.759\ +\ 31^\circ\ 16'\ 03''.94$ ($J2000$) with an epoch of 2001 May 4. The epoch of the 2MASS observations is between the epochs of the VLA observations, and the reported near-infrared coordinates lie between those VLA coordinates. Within the errors of $\pm\ 0''.05$ for the VLA data and of $\pm\ 0''.10$ for 2MASS, and a tentatively indicated small proper motion of VLA 4B, these data show that the near-infrared source SVS 13 is identical to the VLA mm and cm-wavelength source VLA 4B. It should be noted that Anglada, Rodríguez, & Torrelles (2000) and Anglada et al. (2004), on the basis of older optical astrometry, had originally identified SVS 13 with a different cm-radio source: VLA 4A.

We use the distance to NGC 1333 SVS 13 determined by Hirota et al. (2008) from VLBI parallax measurements of masers associated with this object: $235\ \pm\ 18$ pc. The study of the dynamics of the NGC 1333 region by Warin et al. (1996) has determined the systemic velocity of the gas near SVS 13 to be 8 km s^{-1} relative to the local standard of rest. Throughout this paper, we will give velocities relative to this systemic velocity of the NGC 1333 molecular core that SVS 13 is embedded in.

Young, still accreting stars often experience eruptive changes in brightness that traditionally get classified into either FU Orionis (FUor) or EX Lupi (EXor) type outbursts, depending on the duration of the outburst and its spectrum. The first review of these phenomena has been given by Herbig (1977). FUor outbursts exhibit time scales of decades to centuries and the spectral characteristics of an optically thick luminous disk with absorption line spectra, while the less substantive EXor outbursts have timescales of years, have been observed to actually return to pre-outburst brightness, and show optically thin emission line spectra. Jets emanating from young stars are often comprised of a series of individual shock fronts that have been postulated to arise from changes in the jet velocity as a result of repetitive eruptive events, as described in the review by Reipurth & Bally (2001) and references therein. This gives, in principle, a way to study the history of such eruptive accretion instabilities from the "fossil" record in the jet shock fronts. Our target object, SVS 13, is certainly in this class of multi-shock outflow sources and has been observed to undergo an outburst around 1990, but the light curve does not match either the classical FUor or EXor curves. The relationship of this last observed outburst to the structure of the

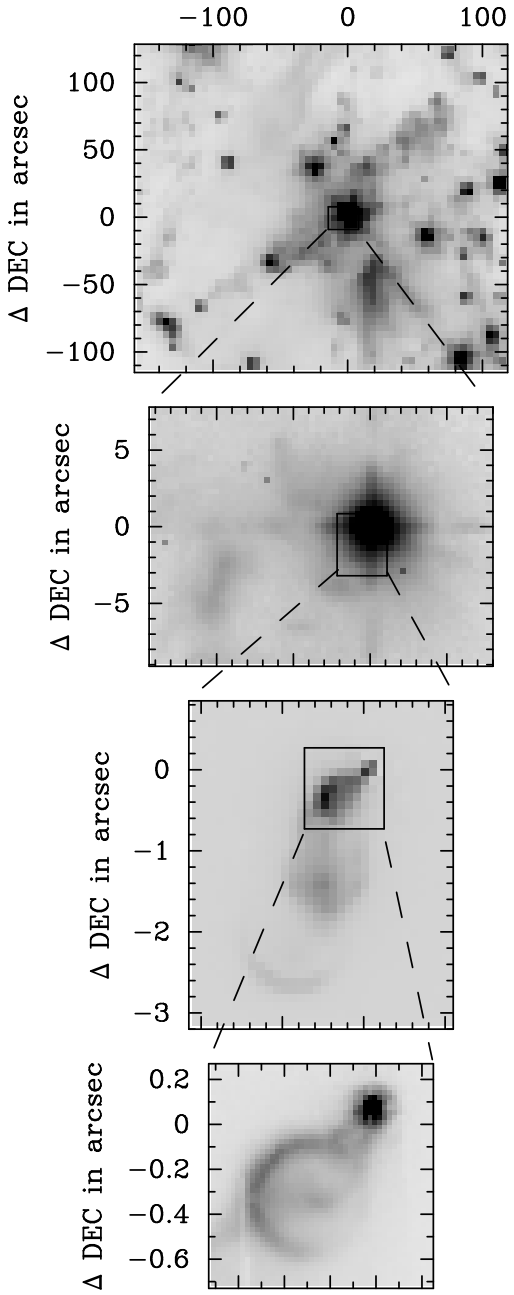

Fig. 1.— The SVS 13 outflow at four different spatial scales: The top image is a Spitzer channel 2 (4.5 μm) image based on the same original data as those used by Raga et al. (2013) for their proper motion study. The image shows the full extent of the shocked molecular hydrogen emission. The second panel from the top is a small portion of a H_2 S(1) 2.122 μm image obtained in 1996 with the QUIRC camera at the UH 2.2 m telescope that shows the emission features closest to SVS 13. The third panel shows the integrated H_2 S(1) line intensity observed with OSIRIS on Keck II in 2011 with the 100 mas spaxel scale, while the fourth panel was taken with OSIRIS on Keck I in 2012 with the 20 mas spaxel scale.

SVS 13 outflow will be studied here.

The proper motions of the shock fronts of the HH 7-11 system associated with SVS 13 have been studied at optical wavelengths by Herbig & Jones (1983) and later by Noriega-Crespo & Garnavic (2001), and in the infrared in the H_2 1–0 S(1) line by Noriega-Crespo et al. (2002) using the Near-Infrared Camera and Multi-Object Spectrometer (NICMOS), by Khanzadyan et al. (2003) using the United Kingdom Infrared Telescope (UKIRT), and with the Spitzer Space Telescope by Raga et al. (2013). These studies all gave proper motions of the shock fronts in the range of 33 mas yr^{-1} that establish a kinematic expansion age of 2100 yrs for the most distant shock front studied there, the HH 7 bow shock.

In general, the jets seen in optical and near-infrared forbidden lines, mostly in [SII] and [FeII], offer the most direct view of the material ejected from an accretion disk or from a protostar's magnetosphere. There are differences in the details of theoretical models of this process, e.g., in Camenzind (1990), Ferreira (1997), Königl & Pudritz (2000), or Shu et al. (2000), but they all agree on the main point: Jets originating from the magnetosphere of a rotating star, or from a rotating disk, and detected in high-excitation shock-excited lines are expected to carry away excess angular momentum and thereby enable the mass accretion process.

However, to date, the most convincing detection of a rotational signature of jets from very young and still deeply embedded objects in SED classes 0 and I have been obtained with radio interferometric observations of outflows in CO and SiO emission. These observations typically achieve spatial resolutions of a few arcseconds but make up for this disadvantage by exquisite velocity resolution. Carbon-Monoxide high-velocity emission is mostly associated with the entrainment of ambient molecular material into a jet originally emitted at even higher velocity. Any signature of the original jet rotation is expected to be highly confused at this turbulent interface between the jet and the ambient material. Nevertheless, Launhardt et al. (2009) detected the kinematic signature of rotation in the jet of CB 26 in the CO(2-1) line, very close to the source of the jet. Zapata et al. (2010) found some evidence for rotational components in the Ori-S6 outflow using various higher transitions of CO and SO, while Pech et al. (2012) recently reported a rotational signature in the HH 797 outflow in IC 348 using CO(2-1). In these cases, the strongest rotational signatures were found at some distance ($\approx 1''$) from the driving source. Even farther away from the driving source, using SiO data from the VLA, Choi et al. (2011) found a rotation signature of the NGC 1333 IRAS 4A2 protostellar jet, consistent with the disk rotation in that object. The jet could only be observed at distances of more than $5''$ from its source, and the rotation signature appears most pronounced at distances of $20''$. These results are far from universal, however. In a series of papers on HH 211 culminating in Lee et al. (2009) they obtained

only a tentative detection of rotation. Codella et al. (2007) studied the kinematics of SiO emission in the HH 212 jet and did not detect a credible rotational signature. In this paper we have tried to detect the kinematic signature of jet rotation in our [FeII] data and are presenting our velocity data, but in the end failed to detect this effect.

2. OBSERVATIONS

2.1. Keck Adaptive Optics Imaging Spectroscopy

There are two strong systems of near-infrared emission lines that are commonly used for the study of protostellar jets: the ro-vibrational lines of H_2 and the forbidden [FeII] lines. As was already discussed specifically in the case of SVS 13 by Takami et al. (2006), the H_2 lines, the brightest being the 1–0 S(1) line at 2.122 μm, trace low-velocity shocks, either internal shocks within the jet, or the turbulent interface to the ambient medium around the jet. This line is therefore well suited for the study of internal shocks and entrainment of ambient material by the jet, but is less suited for a detection of the jet itself.

In contrast, [FeII] traces higher temperatures and excitations and is usually confined to the densest parts of a jet near its launch region, and to its terminal shocks against ambient material. The [FeII] lines in the near-infrared are therefore particularly suited for a study of the kinematics of the jet itself. Emission from atomic hydrogen, in the near infrared specifically the Brackett series of lines, is observed in many young stars, and typically originates in the spatially unresolved accretion disk around the young star itself, and not in the jet.

The adaptive optics data reported here were obtained at the Keck I and II telescopes, using laser guide star adaptive optics in conjunction with the OH-suppression Infrared Imaging Spectrograph (OSIRIS) built by Larkin et al. (2006). OSIRIS is a lenslet integral field spectrograph where each spatial element (spaxel) forms an image of the telescope pupil before being dispersed into a spectrum. This technique separates spatial flux gradients in each spaxel from any velocity shifts and is therefore very suitable for measuring small shifts in line centroid over extended objects with spatial scales of the order of a spaxel. The spectral lines mentioned above can be observed in two setting of OSIRIS. In the 3^{rd} grating order and through the Kn2 filter, the H_2 S(1) line at 2.122 μm is covered. In the 4^{th} grading order and through the Hn3 filter, two [FeII] lines and two Brackett-series lines are included in the spectral bandpass.

The first observations were carried out in the night of 2011 August 21, (UT) (MJD 55794.5345 = 2011.638) with OSIRIS on the Keck II telescope, using the relatively coarse

100 mas per spaxel and 50 mas per spaxel scales and the Kn2 and Kbb filters. A second, higher quality set of data was obtained in the night of 2012 November 4, (UT) (MJD 56235.4853 = 2012.844) with OSIRIS now at the Keck I telescope. The finest of the spaxel scales of OSIRIS, with lenslets subtending 20 mas was used under conditions of exceptionally good seeing, with the Canada-France-Hawaii Telescope (CFHT) seeing monitor reporting average seeing at optical wavelengths of $\approx 0\farcs3$. A third set of data was obtained on 2013 November 22 and 23 (MJD 56618.5 and 56619.5, midpoint=2013.893) with OSIRIS at the Keck I telescope. The seeing was not quite as good as in the year before, but still, very good data were obtained that are well suited for an astrometric comparison with the 2012 data.

Date	*Telescope*	*Grating*	*Filter (λ range)*	*Scale*	*Int. Time*	*FRP*
2011 Aug 21	Keck II	old	Kn2 (2.04 - 2.14)	50mas	1×300s + 1 sky	old
2011 Aug 21	Keck II	old	Kbb (1.97 - 2.38)	100mas	1×300s + 1 sky	old
2012 Nov 04	Keck I	old	Kn2 (2.04 - 2.14)	20mas	4×600s + 1 sky	new
2012 Nov 04	Keck I	old	Hn3 (1.59 - 1.68)	20mas	8×600s + 2 sky	new
2013 Nov 22	Keck I	new	Kn2 (2.04 - 2.14)	100mas	4×300s + 1 sky	new
2013 Nov 22	Keck I	new	Kn2 (2.04 - 2.14)	20mas	4×600s + 1 sky	new
2013 Nov 22	Keck I	new	Hn3 (1.59 - 1.68)	20mas	4×600s + 1 sky	new
2013 Nov 23	Keck I	new	Kn2 (2.04 - 2.14)	20mas	4×600s + 1 sky	new

Table 1: Log of the Keck OSIRIS Observations

On 2012 Nov. 04 and 2013 Nov. 22, we obtained data sets with 600 s individual exposure time in the Hn3 filter, covering the 1.644002 μm $a^4D_{7/2}$ – $a^4F_{9/2}$ emission of [FeII] (referred in the following as the 1.644 μm line) and also the fainter [FeII] $a^4D_{3/3}$ – $a^4F_{7/2}$ line at 1.599915 μm (in the following called the 1.600 μm line). All wavelengths given in this paper refer to vacuum and the line wavelengths and identifications are based on Aldenius & Johansson (2007). Fig. 2 shows a raw spectrum of SVS 13 in the Hn3 filter, averaged over a large $0\farcs2\times0\farcs2$ box centered on SVS 13, to include the radiation from the object, but also the OH airglow sky flux used for wavelength calibration. The [FeII] 1.600 μm line was evaluated and generally corroborates the conclusions drawn from the 1.644 μm line, but due to its lower signal-to-noise ratio, these data are not presented here nor did we try to extract information on excitation conditions from a comparison of those two [FeII] lines. Takami et al. (2006) have already presented a detailed study of the excitation conditions of H_2 and [FeII] emission in SVS 13. In addition to these shock-excited forbidden lines, OSIRIS in 4^{th} grating order with the Hn3 filter also covers two atomic hydrogen emission lines, the 13-4 (1.611373 μm) and 12-4 (1.641170 μm) recombination lines of the Brackett series (Kramida et al. 2012). In the Kn2 filter, 4 data sets with 600 s exposure time each were obtained that cover the H_2 1–0 S(1) line at 2.121833 μm (Bragg, Brault, & Smith 1982).

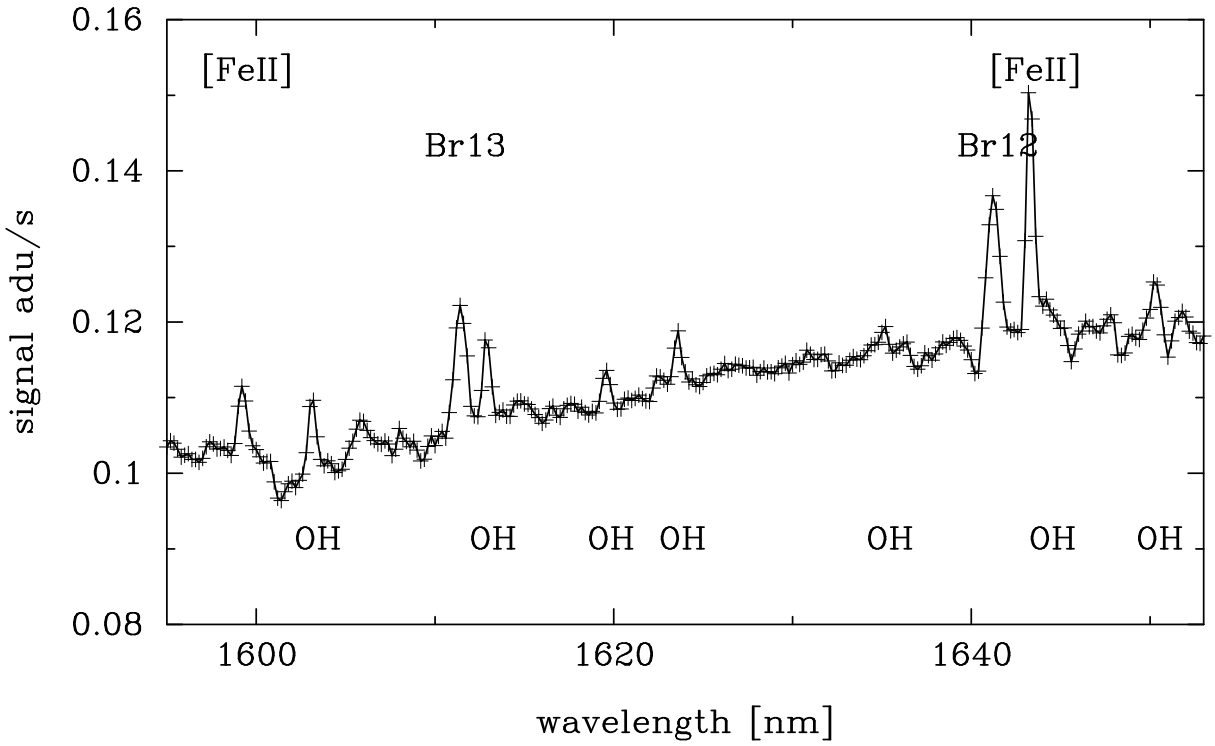

Fig. 2.— Raw spectrum extracted from the OSIRIS data cube in a 0.″2×0.″2 box containing SVS 13, but also substantial sky OH airglow flux. This figure serves to illustrate the Hydrogen Br 12 and 13 lines, the [FeII] lines, and the night-sky OH airglow lines used for wavelength calibration.

2.2. IRIS Photometric Monitoring

For the monitoring of SVS 13 at infrared wavelengths, the brightness of the object around K=8 is actually a problem. Most archival infrared images obtained with large telescopes and modern infrared cameras are saturated on SVS 13. From 2012 to 2014, we have therefore monitored the NGC 1333 region, including SVS 13, with the Infrared Imaging Survey (IRIS) system specifically to study the variability of that object at the present epoch. IRIS is a 0.8 m telescope and 1024×1024 infrared camera dedicated to the monitoring of infrared variability. It has been described in detail by Hodapp et al. (2010).

The IRIS infrared camera, which is a refurbished version of the UH Quick Infrared Camera (QUIRC) described by Hodapp et al. (1996b), is operated in a mode where after the first non-destructive read of the detector array we immediately take a second read, and compute a double-correlated image with only 2 s exposure time by differencing these first two reads. After this second read-out, the integration continues up to a third read of the detector array, which gives the full integration time of 20 s usually used for our monitoring projects. The first (2 s effective integration time) images are far from saturating on SVS 13 and were used for the photometry presented here. The IRIS camera raw data are processed in a reduction pipeline based on the Image Reduction and Analysis Facility (IRAF) software (Tody 1986). The astrometric solution of the co-added images is calculated based on SExtractor (Bertin & Arnouts 1996) and SCamp (Bertin 2005). Photometry is obtained with the IRAF task PHOT and calibrated against the 2MASS catalog (Skrutskie et al. 2006).

3. Data Reduction

3.1. Keck OSIRIS Data Reduction Pipeline

We chose to correct dark current and other signal-independent detector artifacts in OSIRIS by subtracting the median of 10 dark frames of 600 s exposure time from each object exposure, in order not to waste observing time on frequent observations of an empty sky field for sky background subtraction. The 2D detector frames were then processed into 3D spectral data cubes with the OSIRIS final data reduction pipeline (FRP). This process of extracting the spectra from the raw detector format is obviously critical for the wavelength calibration of the spectra and therefore for the extraction of velocity information. In 2013, the Keck Observatory released a new version of the data reduction pipeline (DRP v3.2) with newly calibrated "rectification matrices" that contain the parameters for the extraction of individual spaxel spectra from the raw detector format into wavelength calibrated spectra. A first inspection of the newly reduced 2013 data showed better consistency of the wavelength

calibration across all spaxel and therefore the 2012 data were also re-reduced with the new software and calibration data. These newly reduced data did indeed change the velocity structure observed in the SVS 13 jet to the point of forcing a different conclusions.

The individual data cubes in the Hn3 filter were cleaned of spurious bright spaxels using the IRAF COSMICRAY task on individual planes of the data cube. All data cubes in the Hn3 filter were spatially mosaicked together with offsets determined by the centroid of the bright continuum image of the SVS 13 star. For the shorter wavelengths, this method resulted in superior image quality compared to using offset data supplied by the AO system. For the longer wavelength spectra in the Kn2 band, where we only took one dither pattern, relying on the offsets provided by the laser guide star system proved sufficient. For both the Hn3 and Kn2 data cubes, the individual planes (wavelengths) of the resulting combined spectral data cubes were adjusted for zero sky background using the background zero adjustment in the IRAF task IMCOMBINE. The primary purpose of this procedure was to remove the OH(5,3)R_1(2) night sky line at 1.644216 μm that partly overlaps with the [FeII] 1.644002 μm line, as was discussed by Davis et al. (2003). The integral field spectrograph OSIRIS records all wavelength planes simultaneously, so that the PSF at continuum wavelengths is recorded under identical atmospheric conditions than the structure at emission line wavelengths. Over small wavelength intervals where the wavelength-dependence of diffraction is negligible, very precise continuum subtraction can be achieved. The continuum adjacent to a given line was computed as the average of approximately 10 wavelength planes outside of the line profile and centered on the line.

3.2. OSIRIS Spaxel Scales and Image Orientation

Between the 2011 and 2012 runs, the OSIRIS instrument was moved from the Keck II telescope to Keck I. Both telescopes and their adaptive optics systems have nominally identical focal lengths, but for an astrometric comparison of data from these two telescopes, the spaxel scale in OSIRIS should be observationally verified. The best data available for this purpose were kindly provided by T. Do and J. Lu from their work on astrometry of stars near the Galactic Center where they calibrated OSIRIS astrometry relative to astrometry with NIRC2, an instrument that stayed at the Keck II telescope. These data indicate that at Keck I, the spaxel scale in mas pixel^{-1} of OSIRIS is 1.28% larger than it had been at Keck II. While installed on Keck I, between our 2012 and 2013 observing runs, the grating of OSIRS was also changed, resulting in a new wavelength calibration. Also, as was discussed above, the data reduction pipeline used at Keck for OSIRIS data was upgraded. Finally, in moving from Keck II to Keck I, the optical path leading to OSIRIS now contains one less mirror

reflection, leading to a change in parity of the images. We used the OSIRIS camera with its wider field to obtain a few images tying the OSIRIS spectral data cubes astrometrically to conventional images of SVS 13 and one detectable star in its vicinity. In addition, we observed other objects to ascertain that our data are presented in the correct parity and orientation on the sky.

The precise scale ratio of the nominal 50 mas (used in 2011) and 20 mas (used in 2012 and 2013) spaxel scales of OSIRIS was measured on setup data cubes obtained in 2008 while observing the $\approx 0\farcs25$ separation binary σ Orionis (Hodapp et al. 2009). By averaging the component separation measured in each continuum data cube plane within $\pm$ 0.1 μm of 2.122 μm, a ratio of 2.4534 ± 0.0005 between the two spaxel scales was measured. This value deviates by about 1 % from the nominal scale ratio of 2.5. It should be noted that these deviations from the nominal spaxel scale ratios and the, even smaller, errors of this measurement are much smaller than the astrometric effects of shock-front motion and expansion discussed later in this paper.

3.3. Lucy-Richardson Deconvolution

The continuum images near the emission line features show nothing but the unresolved stellar object SVS 13. They are thus suitable as a PSF kernel for deconvolution of the individual (wavelength) cube planes. The deconvolution was done with the Lucy-Richardson algorithm (Richardson 1972) and (Lucy 1974), as implemented in the IRAF STSDAS package. How fast the Lucy-Richardson algorithm converges depends on the signal-to-noise ratio in the frame. We have tried out different numbers of iterations and chi-square criteria and have chosen a combination that leads to a significant improvement in the spatial resolution without creating obvious artifacts. Working with the original data without continuum subtraction led to strong artifacts in the wings of the overwhelmingly bright stellar source. For the deconvolution of faint emission features well separated from SVS 13 we have therefore worked from the continuum-subtracted data. For the purpose of the grey-scale and RGB representations of the images, we have computed a "high-dynamic-range" version of the image by adding the deconvolved continuum-subtracted image and a small fraction of the image flux of the original deconvolved image, effectively creating an image where the continuum source is strongly suppressed, but still indicated in the image. Fig. 3 shows the S(1) image from 2011 in greyscale, and false color representations of the deconvolved "high-dynamic-range" 2012 and 2013 data in the H_2 S(1) line (red), [FeII] 1.644μm (green) and continuum (blue). Fiducial marks are included to illustrate the expansion of the S(1) bubble over the course of those 2 years.

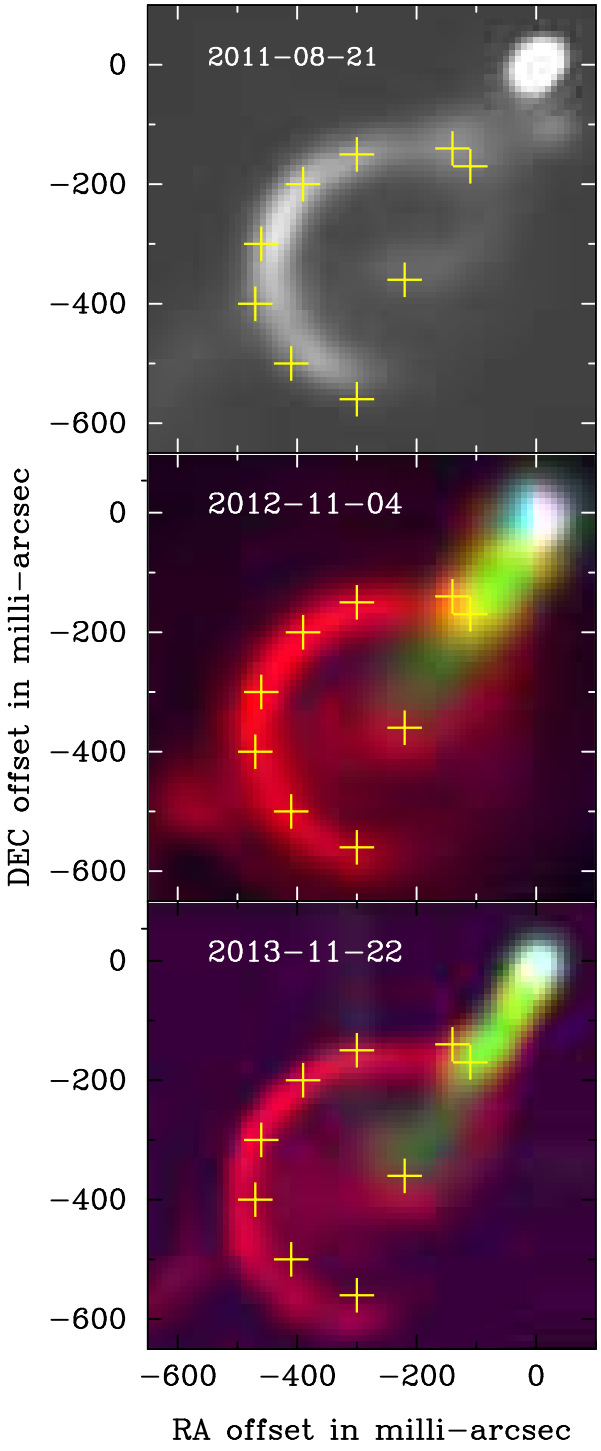

Fig. 3.— The SVS 13 bubble in 2011, 2012, and 2013. False color images composed of the deconvolved and continuum-subtracted H_2 S(1) image (red channel) and the continuum subtracted [FeII] emission line image from 2012 Nov. 4. All three images are aligned to better than 1 mas, even though the deconvolution residuals in the continuum subtracted images do not align precisely. To mark the position of the continuum source SVS 13, the blue channel shows 10% of the continuum near the [FeII] line. A few fiducial marks indicate positions of the bubble rim in 2012. The comparison of these marks to the images taken earlier and later clearly indicated the expansion motion of the bubble.

3.4. Spectral Resolution and Wavelength Recalibration

The OSIRIS final data reduction pipeline (FRP) extracts the data from the raw 2-dimensional detector frame and forms a spectral data cube with 0.2 nm spacing in the H band (4^{th} grating order) and 0.25 nm in the K band (3^{rd} grating order). The OH airglow lines in the bandpass of the Hn3 and Kn2 filters give an opportunity to check the wavelength calibration and to measure the spectral resolution In particular, the OH(5,3)R_1(2) line at 1.644216 μm is very close to the wavelength of the [FeII] 1.644 μm line. For the analysis of the [FeII] line emission, the uniformly distributed OH emission was eliminated by adjusting the spatial median of the flux in the image to zero. In contrast, for the wavelength calibration, the original data were used and the flux in the OH line was measured. To account for continuum stray light, a continuum subtraction using the same continuum as for the [FeII] line extraction was used. The individual OH airglow lines were measured by summing up the flux of 400 pixels without detectable object flux, and measuring the position and width of the OH airglow lines in the resulting one-dimensional spectrum using the IRAF task SPLOT. We used the vacuum wavelengths of OH lines given by Rousselot et al. (2000) and found that the wavelength calibration provided by the OSIRIS reduction pipeline required a slight correction in zero point and dispersion, of order 0.01 nm. After this correction, the individual OH line positions have residual wavelength errors of 0.008 nm, about a factor of two larger than the fit residuals given by our wavelength reference, Rousselot et al. (2000). The OH airglow lines are, in reality, close doublets with line spacing well below the resolution of OSIRIS. The measured FWHM of the OH lines was 0.44 ± 0.06 nm in the Hn3 filter, and 0.61 ± 0.06 nm in the Kn2 filter, a little more than two wavelength planes in the OSIRIS data cubes. Near the [FeII] line at 1.644 μm, one wavelength interval of the data cube corresponds to 37 kms^{-1} in radial velocity. The spectral resolution near that line therefore corresponds to 81 kms^{-1}. Near the H_2 1–0 S(1) line at 2.122 μm, one wavelength interval of 0.25 nm corresponds to a radial velocity difference of 35 kms^{-1}, and the measured FWHM of the spectral lines corresponds to 85 kms^{-1} width of the spectral profile. Most of the velocity effects discussed in this paper are therefore smaller than one spectral resolution element. The accuracy of velocity measurements depends on the signal-to-noise ratio of the emission in question. In our discussion of the velocity structure of the [FeII] microjet in section 4.5, we will present a detailed analysis of the measurement errors in that particular case.

3.5. No Telluric Absorption Correction

We have taken data on an A0V star during the observations, but in the end have chosen not to use these for telluric absorption correction. Our data analysis does not rely

on spectrophotometric correction of the data cubes. In the Hn3 filter, the study of the jet in the 1.644 μm [FeII] line and of the HI13-4 and HI12-4 Brackett lines are potentially all affected by the broad atomic hydrogen absorption in the standard star, and the data reduction pipeline would therefore interpolate through the hydrogen lines, making the telluric absorption correction meaningless at these wavelengths.

We have also not been able to use those standard star measurements for a flux calibration of our spectra. A consistency check of data obtained with different exposure times showed a problem with the way OSIRIS computes the effective integration times for multi-sampled exposures. We do not have the data to fully calibrate this effect, and given that the flux calibration is not essential for our data analysis, prefer not to give a flux calibration for our data.

4. Results and Discussion

4.1. The SVS 13 Outflow on Different Spatial Scales

Figure 1 shows the H_2 shock-excited line emission associated with SVS 13 on four different spatial scales: The top image is an archival Spitzer Space Telescope Infrared Array Camera (IRAC) (Fazio et al. 2004) channel 2 (4.5 μm) image covering most of the outflow emission. The second panel is a small cutout from a ground-based, seeing limited image in the H_2 1–0 S(1) line obtained at the UH 2.2m telescope, showing just the emission in the immediate vicinity of SVS 13. The third panel from the top is the S(1) integrated line image obtained with the 100 mas scale of OSIRIS in 2011 and the bottom panel shows the 20 mas scale S(1) image from OSIRIS obtained in 2012, without deconvolution. We show this figure to demonstrate the relationship between the bubbles in the SVS 13 outflow very close to the source and the larger scale structure of the flow further downwind. This relationship is not entirely trivial, since not all the bubbles have propagated in the same direction from the SVS 13 star. The seeing-limited ground-based image shows the brightest of these bubbles in the glare of the PSF. The intermediate, 100 mas scale, OSIRIS line image shows three distinct partial bubbles near the source of the outflow, the outer two of which were also observed, but not further discussed, by Noriega-Crespo et al. (2002), on HST/NICMOS images and had also been detected through UKIRT narrow-band Fabry-Perot imaging by Davis et al. (2002). The best prior detection of these bubbles was by Davis et al. (2006) who used adaptive-optics-assisted long-slit spectroscopy and detected all the bubbles as a series of emission maxima along the slit.

The most recent emission, the 0.″2 long [FeII] jet, its faint extension into the S(1) bubble,

and that youngest S(1) bubble are oriented at P.A. 145°, as seen in Fig. 3. The older two bubbles, visible in the 100 mas image of Fig. 1, are lying more to the south at P.A. 159° than those aforementioned features, indicating some variations in the jet emission direction. In contrast the main chain of Herbig-Haro knots HH 7-11 lies at P.A. 123° (Davis et al. 2001).

While at optical wavelengths, the SVS 13 outflow manifests itself only in the Herbig-Haro chain HH 7-11 (Herbig & Jones 1983), longer wavelengths increasingly reveal a counterflow that appears displaced from the HH 7-11 axis, and appears in general fainter and less organized (Fig. 1, top panel). Based on Spitzer telescope images over a time span of 7 years, Raga et al. (2013) have obtained one proper motion data point for a relatively well defined knot in that counterflow, and this one point is consistent with the counterflow originating from SVS 13. Also, no other embedded protostar has been detected by Walsh et al. (2007) to the north of SVS 13 that might explain this flow as being independent from SVS 13. The displacement in the outflow axis, in combination with the recent changes in outflow direction reported in this paper, suggest that the source of the SVS 13 outflow is changing direction, probably due to some precessing motion, as will be discussed in more detail in section 4.2. As an explanation for the differences between the HH 7-11 flow and the counterflow, Walsh et al. (2007) have suggested that the northern counterflow enters into the central cavity of NGC 1333, resulting in different ambient pressure and excitation conditions than the HH 7-11 flow.

4.2. H_2 Shock Front Proper Motions

We have obtained astrometry of the bubble expansion on two different spatial scales. Relatively wide field OSIRIS data cubes with the 100 mas spaxel^{-1} scale were obtained on Keck II on 2011 August 21 and Keck I on 2013 November 23. A difference image of the H_2 S(1) emission at these two epochs is shown in Fig. 4 and illustrates that all three of the closest shock fronts to SVS 13 are showing noticeable motion. The farthest of these three shock fronts was defined enough to allow a cross-correlation measurement of its expansion age in the box indicated in the figure.

Astrometry of the smallest and youngest expanding bubble was done on the 2012 November 4 and 2013 November 22/23 data that were taken at the Keck I telescope with the same adaptive optics system and the same spaxel scale (20 mas spaxel^{-1}) and are therefore suitable for a precise astrometric measurement. In this case, the individual planes of the data cube were deconvolved using the Lucy-Richardson algorithm, to improve the definition of the bubble edge. Figure 3 illustrates the expansion and motion of the youngest, smallest bubble between the three epochs by superposing fiducial marks that outline features in the

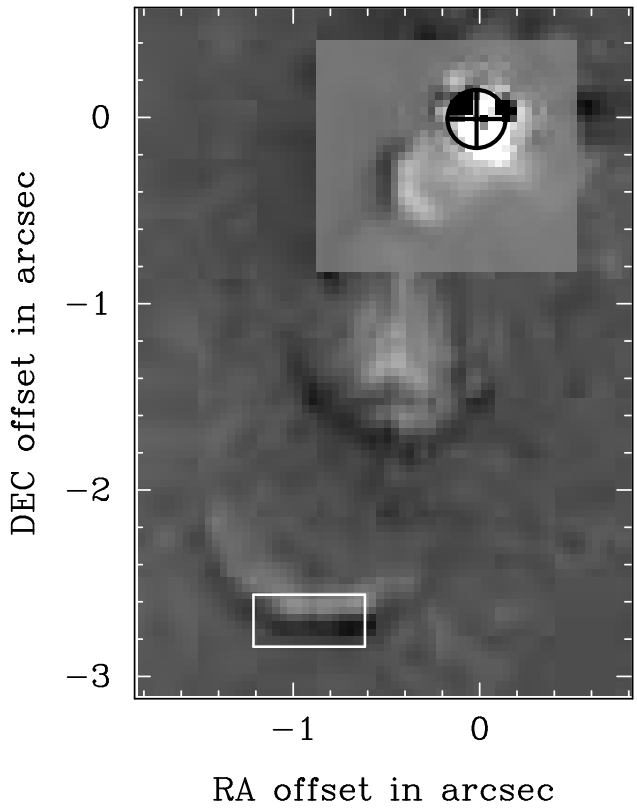

Fig. 4.— Difference frame of the 100 mas scale images taken in 2011 and 2013. The cross-correlation box for the most distant shock front is indicated. The insert shows the inner (youngest) bubble and the subtraction residuals of SVS 13 in different flux scaling. The scaling is such that bright pixels in the frame show more flux in 2011 than in 2013. All three shock fronts therefore show the signature of expansion with the dark (2013) features farther away from SVS 13 than the bright (2011) features.

middle (2012) image.

For fine registration of the images, the IRAF task XREGISTER was used to measure the relative alignment of all the frames at the position of the SVS 13 stellar object and a magnified and optimally registered version of the images was produced. To measure the expansion of the bubble, we worked under the assumption that its motion relative to the star can be described as a simple constant velocity expansion with the origin at the position of the star. We computed magnified versions of the individual 2012 November 4 images with magnification factors in the range from 0.95 to 1.10 and the center of the magnification on the SVS 13 star. We then computed the product of these magnified images and each of the individual 2013 November 22 images. The average of this product in a box centered on the S(1) bubble feature image varies smoothly with expansion factor for each of these pairs and the maximum of this one-dimensional correlation function was simply read from the table of cross-correlation values. We show the cross-correlation functions of the 2012 and 2013 high resolution images in Fig. 5 to illustrate the variations due to noise and deconvolution noise amplification, and to document how the errors of this measurement were obtained.

The expansion factor so determined was then converted to a kinematic expansion age of 32 yrs (prior to 2012), i.e., kinematic starting time of the expansion in 1980, which gives the upper limit to the true age of the bubble assuming that the bubble has been expanding at constant velocity. Since, realistically, the bubble is expanding into the dense environment of a molecular core, the true age of this youngest bubble will be smaller than the kinematic expansion age and is therefore consistent with this expanding bubble having been generated in the 1990 photometric outburst of SVS 13 that will be discussed in secion 4.4. In 2012, the apex of the bubble was located 654 mas from the star. The front end of the bubble therefore has moved with an average projected angular velocity of 20 mas yr^{-1} (4.7 AU yr^{-1} = 22.3 km s^{-1} at 235 pc distance) away from the star. Similarly, in 2012, the bubble had a radius of 212 mas and an average radial proper motion of 6.6 mas yr^{-1} (1.55 AU yr^{-1} = 7.35 km s^{-1}). The proper motion of the bubble center is therefore the proper motion of the leading shock front minus the radial expansion: 13.4 mas $yr^{-1} \approx 15$ km s^{-1}.

In order to also obtain an estimate of the kinematic age of the next two more distant bubbles, we used data cubes obtained in 2011 August 21 on Keck II with the 100 mas scale, and similar measurements obtained on 2013 November 22 on Keck I. The difference of these two images is shown in Fig. 4. The only shock front where a clear maximum of this correlation function was detected in these 100 mas data was the most distant of the three, indicated by a box in Fig. 4, separated from the star by 2.87″ in 2011. For this bow shock front, we derive a kinematic formation time of 1919 ± 7 and a linear projected proper motion of 31 mas yr^{-1}. We have not obtained a reliable kinematic age for the middle shock-excited

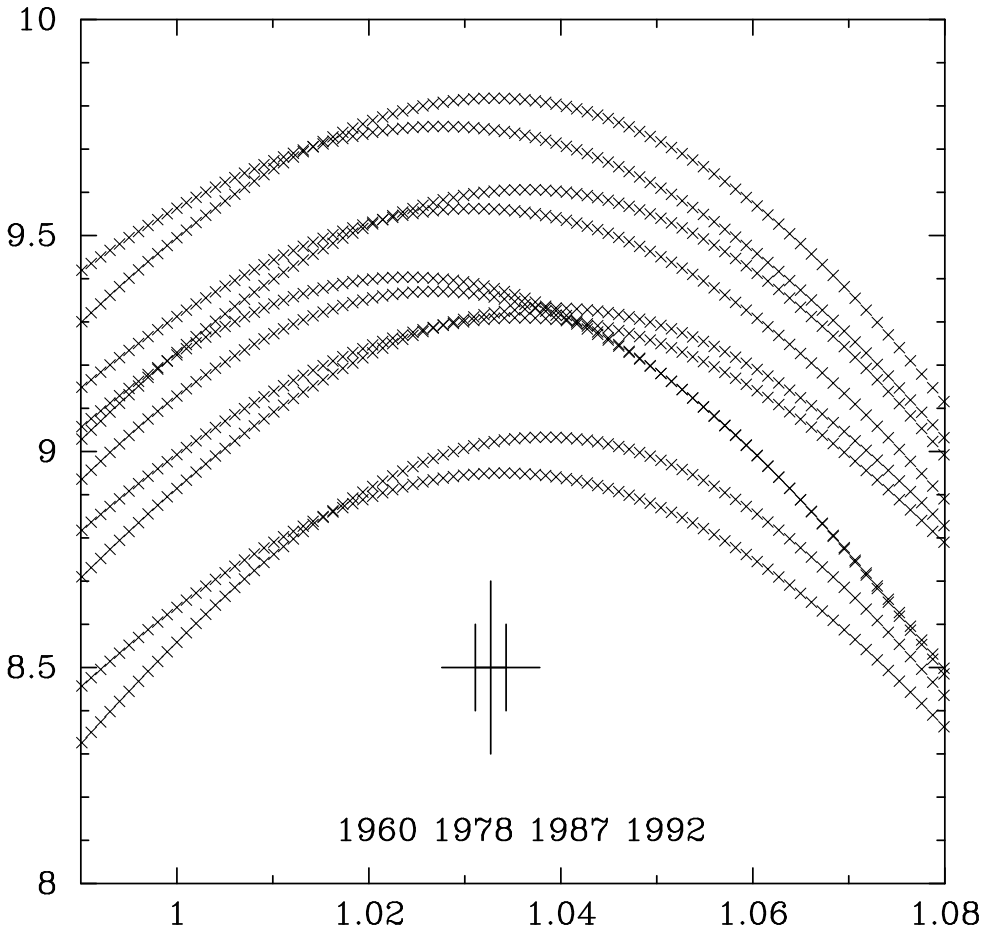

Fig. 5.— The 10 individual cross-correlation results between individual 2012 and 2013 images taken with the OSIRIS 20 mas spaxel scale. The horizontal axis is the expansion factor of the 2012 data to match the 2013 data, and the vertical axis is the average of the product of the two frames, i.e., the cross-correlation function. The expansion starting dates corresponding to the expansion factors are also indicated. The error bars indicate the 1 σ error of the mean scaling factor. The mean value corresponds to a kinematic start of the expansion in 1980, an early limit to the true starting date since the expanding bubble will realistically be decelerated.

feature at $\approx 1\farcs5$ from the star, between those two features discussed above (Fig. 4). The fact that this rather poorly defined system of shock fronts lies pretty precisely in the middle of the 1980 and 1919 (kinematic formation time) features suggests that this feature must have formed, again in the kinematic sense without accounting for deceleration, around 1950. If there is a regular pattern to the formation of these bubbles, which with only three examples cannot be convincingly established yet, the next outburst could be expected within the next decade.

It should be noted, as was already pointed out by Khanzadyan et al. (2003) that the proper motion of the major shock fronts in the older parts of the SVS 13 outflow indicate a much longer time interval between shock front generating events: about 500 yrs. It is not clear whether SVS 13 exhibits multiple periods, or whether the frequency of ejection events has recently increased. An argument for the latter point of view may be that the outflow direction has apparently changed in the past century, as we will discuss now.

As demonstrated by Fig. 1, the two previous bubbles are located more toward the SE of SVS 13 and, for example, Davis et al. (2006) chose P.A. 159° as the best slit orientation to cover them. The larger chain of HH objects 7 to 11 is oriented along a position angle of 123° (Davis et al. 2001). The larger scale proper motion study by Raga et al. (2013) based on Spitzer 4.5 μm images shows some emission knots to the SE of SVS 13 with a proper motion vector generally to the SE, in particular the Herbig-Haro knots 7, 8, and 10. North of SVS 13, in the counter-flow, they find an emission knot with a generally northern proper motion vector (P.A. -10°) that they ascribe to a chance superposition of another outflow far to the south of SVS 13 and with generally northern outflow direction. The [FeII] jet originating from SVS 13 (Fig. 3) is oriented along P.A. 145° and the H_2 bubble center is displaced from SVS 13 along the same angle. With the exception of this most recent H_2 bubble, the other recent mass ejection events from SVS 13 have therefore ejected material initially in a more southerly direction (P.A. $\approx$ 155° - 159°), as seen in Figs. 1, and 4. With outflows generally being bipolar, there must also be mass ejected into a northerly direction. We therefore believe that, contrary to the assertion by Raga et al. (2013), the 4.5 μm emission knot north of SVS 13 and with northerly proper motion is part of the counter jet to the bubbles reported here. The more distant parts of the S(1) emission NW of SVS 13 are anti-parallel, but laterally displaced, from the HH 7-11 system of emission knots. We suggest that the HH 7-11 chain, the system of bubbles immediately south of SVS 13, the emission knots north of SVS 13, and the more distant emission knots further to the NW (Fig. 1) are all part of the same bipolar outflow originating in SVS 13. This outflow has the S-shaped morphology indicative of a precessing or otherwise unstable jet source. Corroborating this, radio interferometry mapping of molecular emission near SVS 13 by Bachiller et al. (2000) has similarly found an orientation of high-velocity material south of

SVS 13 different than the HH 7-11 Herbig-Haro chain. They had already concluded that the differences in the alignment of features of different age indicate a precessing source of the outflow. A prominent other example of such S-shaped morphology of a molecular hydrogen jet, IRAS 03256+3055, is located just south of SVS 13 in NGC 1333 and has been studied in detail by Hodapp et al. (2005).

The relatively low proper motion and spatial velocity measured for the H_2 bubble studied here is consistent with proper motion measurements of the more distant HH 7-11 chain of shock fronts by Herbig & Jones (1983), Noriega-Crespo & Garnavich (2001), and Raga et al. (2013), but is inconsistent with the much higher proper motions reported by Chrysostomou et al. (2000) in the first near-infrared proper motion study of HH 7-11.

While a precessing accretion disk provides an explanation for the rapid changes in the outflow direction observed in SVS 13, our data do not show any indication for the presence of a companion object that would be close enough to cause the disk precession on the timescales discussed here. From the size and location of the H_2 bubbles, we can conclude that bubble ejection events happen with a period of several decades. In the model where such events are triggered by periastron passages of a companion object, the orbital semimajor axis must be of order of tens of AU, or several of the original 20 mas spaxels of our data. The fact that we don't see a companion object implies that such an object, if it existed, is intrinsically too faint and/or too deeply embedded to be visible in the H and K atmospheric windows.

The only other case of a young stellar object with a pronounced bubble structure of its outflow is XZ Tau that was studied in detail by Krist et al. (2008) on the basis of optical multi-epoch HST imaging. Very similar to the case of SVS 13 discussed here, their images show a series of bubbles with a collimated jet propagating inside of the bubbles. Krist et al. (2008) reported initial results of numerical simulations of a very young pulsed jet in close proximity to its driving source. Their simulations were specifically tuned to reproduce the observations of the XZ Tau A chain of bubbles and therefore modeled a faster, more rapidly pulsing jet resulting in more rapidly expanding, overlapping bubbles. The general scenario underlying their model is however applicable to our case of SVS 13: The FUor-like photometric outburst in 1990 created a short-lived pulse of jet activity. This newly created, relatively fast jet ran into slower moving material ejected prior to the outburst event, and this internal shock created an expanding "fireball" that subsequently expanded ballistically into a bubble carried away from the star by the outflow. Some time after the formation of the bubble, a fast continuous jet then emerges to catch up with the bubble, pierce it, and partially destroy it. In SVS 13 this process currently repeats itself about every 30 years, creating the series of bubble fragments that forms the string of Herbig-Haro objects. In distinction from XL Tau, the case of SVS 13 also involves a significant change in the direction of the jet and bubble

ejection leading to the S-shaped overall morphology of the Herbig-Haro chain.

4.3. H_2 Shock Front Radial Velocity

The individual velocity channels of the H_2 S(1) line emission are shown in Fig. 6. In the blue-shifted wing of the velocity distribution, emission projected on the center of the bubble is visible, which is the expected characteristic of an expanding 3-dimensional bubble rather than a 2-dimensional ring. In Fig. 7, a color-coded velocity map of the H_2 1–0 S(1) line emission is presented. The S(1) emission shows three distinguishable velocity features. Emission near the intersection with the jet (traced in [FeII]) shows the smallest blueshifted velocities and is coded red. The rim of the S(1) bubble where the line of sight is tangential to the bubble shows intermediate velocities, coded yellow in the figure. The highest velocities towards the observer are measured in the filamentary features projected against the center of the bubble and are coded in blue. In the brightly visible rim, the velocity centroid varies between -40 and -55 km s^{-1} relative to the systemic velocity of the molecular material around SVS 13, while in the simple model of an expanding shell, those velocities should be constant and representative of the center motion of the bubble. We take -47 $\pm$ 7 km s^{-1} as the typical radial velocity of the bubble center.

With the proper motion of the bubble center of 15 $\pm$ 2 km s^{-1}, this suggests an inclination angle of 18° $\pm$ 3° against the line of sight. Takami et al. (2006) had given an inclination angle of 20° to 40° for emission close to SVS 13 while Davis et al. (2001) has given 40° for more distant emission knots. All the measurements of the inclination angle were done on different shock features. Their spread is therefore a combination of measurement uncertainties and the true variations in the motion of these shock fronts. Irrespective of which of the shock fronts are measures, all data indicate that the outflow emerging from SVS 13 is pointed strongly towards the observer. This explains why the counterjet, which moves away from the observer and into the molecular core around SVS 13, is not detectable at optical wavelengths. Shock fronts of this velocity running into stationary ambient molecular hydrogen are certainly capable of exciting v=1–0 S(1) line emission and are not in danger of dissociating the H_2, see, for example, Draine (1980).

4.4. The Outburst and Light Curve of SVS 13

The infrared source SVS 13 was discovered by Strom, Vrba, & Strom (1976) at a K-band magnitude of 9.08 in a 36″ aperture. Soon after the discovery, Cohen & Schwartz

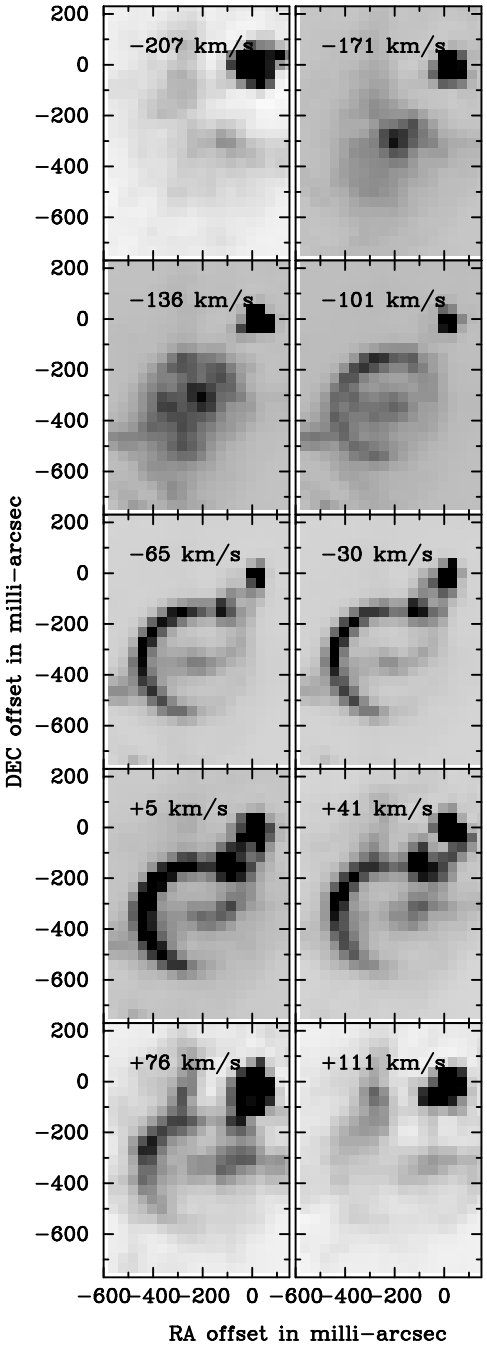

Fig. 6.— Continuum-subtracted H_2 1–0 S(1) line images of the SVS 13 jet. The velocities indicated in each panel are relative to the systemic velocity of the SVS 13 core. The bubble feature is blueshifted relative to the systemic velocity.

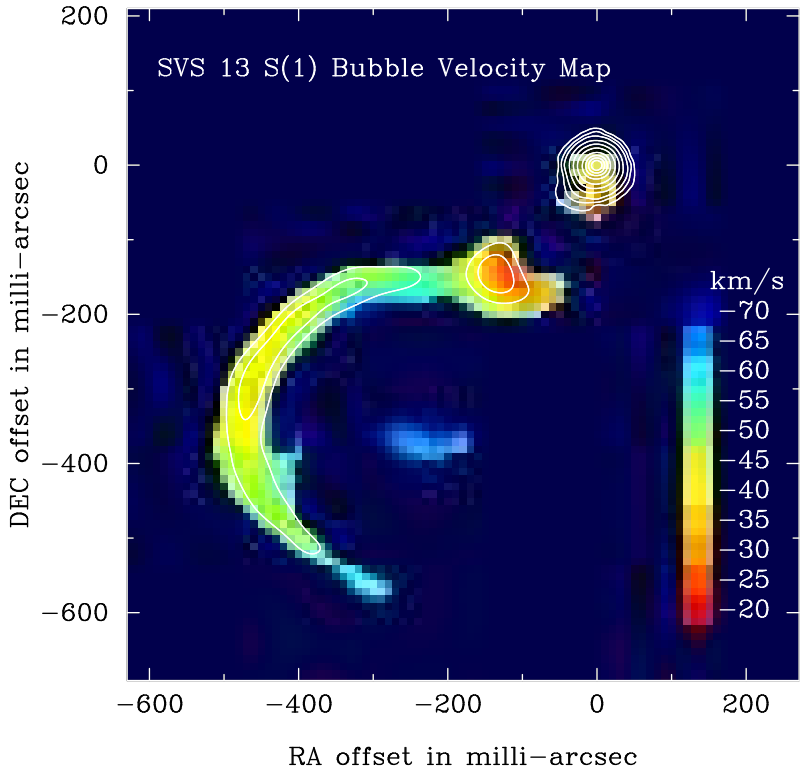

Fig. 7.— Velocity map of the SVS 13 bubble in the H_2 S(1) line at 2.122 μm. Three distinct velocity features can be distinguished: The emission at the intersection of the jet with the bubble has the lowest (blueshifted) radial velocity, The rim of the bubble has intermediate velocities, and the features projected against the center of the bubble have the highest blueshifted velocities. Overlayed on the velocity map are contours of the high-dynamic range Lucy-Richardson deconvolved flux maps that indicate the position of SVS 13 itself. A color version of this figure is available in the electronic version of this paper.

(1980) reported K = 8.48 in a 30″ aperture observed in 1978. Liseau, Lorenzetti, & Molinari (1992) reported an observation by G. Olofsson from 1980 at K=8.7 in a 14″ aperture as a private communication. Harvey, Wiling, & Joy (1984) measured a pre-outburst brightness on K=9.34 in a 6 - 8″ aperture at the IRTF on 1981, Oct. 11-13 and Cohen & Schwartz (1983) measured K=9.30 in a 16″ aperture on 1981, Dec. 3-9.

The object experienced a sudden increase in brightness around 1990, as first reported by Mauron & Thouvenot (1991) and further studied by Eislöffel et al. (1991), Liseau, Lorenzetti, & Molinari (1992), and Aspin & Sandell (1994). In the K band, where the best pre-outburst data are available, as listed above, the pre-outburst magnitude showed some variation between 9.0 and 9.5 mag. Post-outburst, Aspin & Sandell (1994) documented brightness variation between 8.0 and 8.6 mag. Based on the small amplitude of the brightness increase, the post-outburst brightness fluctuation, and the emission lines in its spectrum, both Eislöffel et al. (1991) and Aspin & Sandell (1994) have concluded that SVS 13 underwent an EXor or similar outburst, but both papers left the possibility open that the outburst may be of a different nature. Khanzadyan et al. (2003) has studied the photometric behavior of SVS 13 again and concluded that the object had not returned to its pre-outburst brightness at that time. Motivated by the uncertain classification of this event, we have re-examined the historical photometry and are discussing new measurements. We have tried to gather the available photometric data on SVS 13 from the literature and data archives. While many images of the SVS 13 region exist, the star SVS 13 is saturated on most of these, and useful data can only be obtained from shallow surveys, usually with small telescopes. In Fig. 8, we show all the available photometric data as a light curve.

The 2MASS survey list SVS 13 as K_s=8.169 and these data had been obtained on Nov. 26, 1999. Recent K_s data from the IRIS telescope (Hodapp et al. 2010) show SVS 13 varying in the range of K_s=8.46 to 8.70 between 2012 August and 2014 January. The photometric color transformations between the UKIRT system and the 2MASS system for the K vs. K_s filters are insignificant (Carpenter 2001), so a direct comparison can be made between the measurements by Aspin & Sandell (1994) and the most recent data. There is extended emission around SVS 13, so very large photometric apertures tend to overestimate the brightness. The Strom, Vrba, & Strom (1976), Cohen & Schwartz (1980), Olofsson (1980) and Cohen & Schwartz (1983) data were corrected to the aperture diameter of 6″ used for the IRIS photometry, while all other photometric data shown here were originally obtained with apertures in the range of 5″ - 8″, close enough to the IRIS aperture to not require a correction. Figure 8 shows these aperture-corrected photometric values and clearly demonstrates that SVS 13 has not declined back to its pre-outburst (< 1990) brightness, but remains at or near its peak post-outburst brightness with some indication that brightness fluctuations have diminished over the course of the past 24 years.

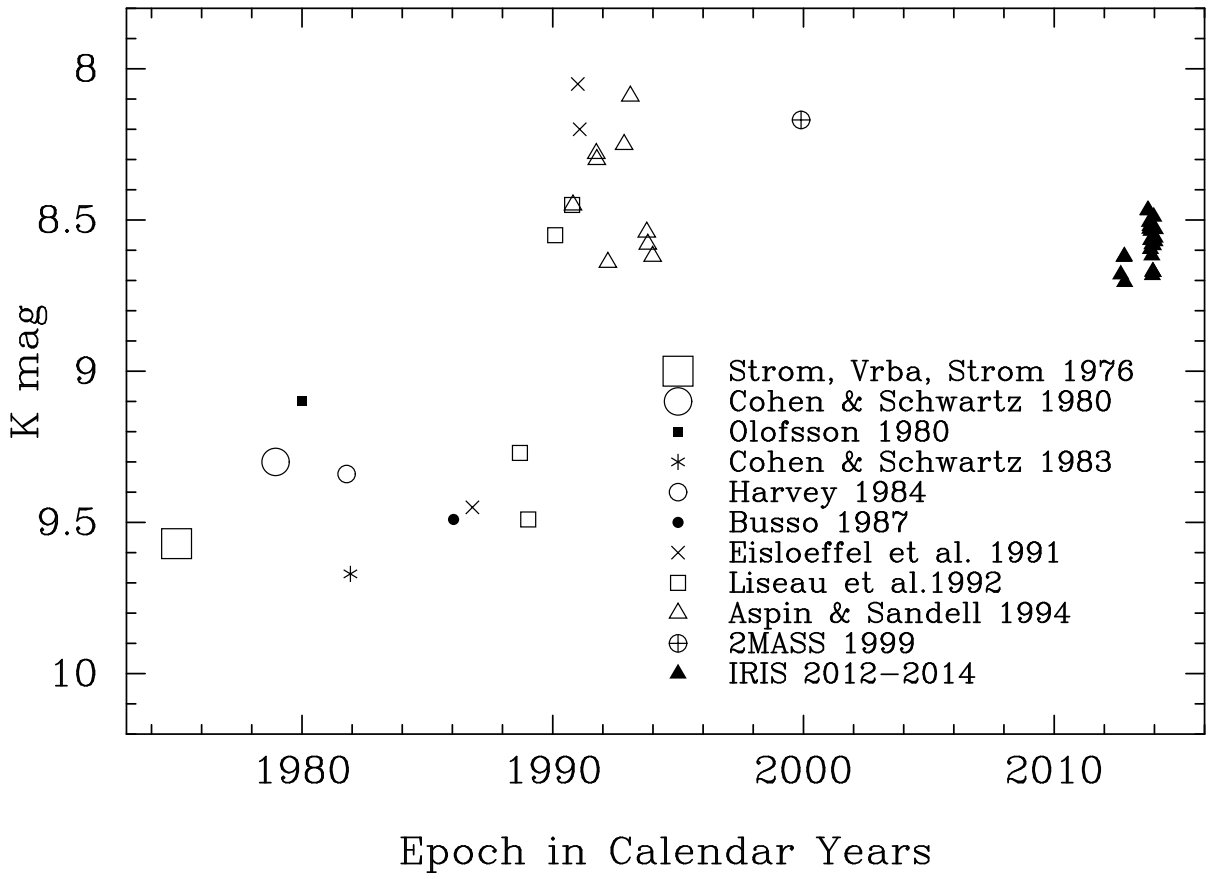

Fig. 8.— The lightcurve of SVS 13 from its discovery in 1974 to the present. This lightcurve is compiled from all published K-band photometry of this source, the 2MASS catalog value, and recent photometry from the IRIS telescope. The four oldest photometry data points have been corrected to match the much smaller photometric apertures used in the more recent photometry based on the flux distribution in present epoch images. The labels give the bibliographic reference, not the epoch of the observations.

Similar to the case of the low-luminosity, deeply embedded, cometary nebula OO Ser (Hodapp et al. 1996a) and (Hodapp et al. 2012), SVS 13 defies a clear classification as either FUor or EXor. While FUors generally show late-type low gravity absorption spectra in the infrared (Greene, Aspin, &Reipurth 2008) indicative of a luminous, optically dense disk, the prototypical EXor EX Lupi shows the CO bandheads and many other optical lines in emission during extreme EXor outbursts (Aspin et al. 2010). During minor outbursts, optical emission lines are observed, but CO may be in photospheric absorption (Herbig et al. 2001). SVS 13 shows the CO bandheads in emission (Takami et al. 2006). In the context of this paper, the important conclusion is that the elevated post-outburst level of accretion and therefore jet activity in SVS 13 has persisted for the past 2 decades to the present, so that the light curve of SVS 13 shares the long duration maximum with FUors, while spectroscopically, it resembles an EXor, and the small outburst amplitude resembles neither. This suggests that at least for the younger, more deeply embedded accretion instability events, the traditional two classes may not be appropriate, and that a continous range of outburst characteristics may be a better way to understand this phenomenon. The light curve also implies that the next outburst of SVS 13, if indeed these outbursts occur repetitively about every 30 years, will start from a brighter state of SVS 13 than the previous one. This would mean that in addition to the repetitive outbursts, we are also observing cumulative changes in SVS 13.

4.5. The [FeII] Microjet

The seeing-limited integral field spectroscopy of Davis et al. (2011) had only marginally resolved the [FeII] emission around SVS 13. Our adaptive-optics corrected OSIRIS data show that [FeII] traces a high-velocity microjet that extends from the source SVS 13 into the area of the most recent molecular hydrogen bubble. The results are summarized in the false-color images (Fig. 3). Here, the wavelength-integrated continuum-subtracted flux of the H_2 1–0 S(1) line was Lucy-Richardson deconvolved and is displayed in the red channel. To show the location of the stellar central object in SVS 13 without introducing the artifacts from imperfect deconvolution of a dominant bright source, we have added 10% of the deconvolved flux of two continuum wavelength channels to the continuum-subtracted image. This produces, in effect, a high-dynamic-range version of the SVS 13 image for the purpose of showing the relationship of features at different wavelengths. Note that the wavelength channels used here were different from those used as the PSF. The resulting deconvolved continuum image is therefore not the trivial solution of deconvolving the PSF with itself. The green channel of Fig. 3 shows the deconvolved integral over the [FeII] line at 1.644 μm. In the same way as described above, a fraction of the continuum wavelengths immediately adjacent to the line was added to the data to mark the location of the stellar source. Finally,

to adjust the color balance of the stellar object to white, the same fraction of the continuum wavelength channels on either side of the [FeII] line was assigned to the blue channel.

Our Lucy-Richardson deconvolved images of the high-excitation [FeII] shocks associated with the jets show that the jet is very narrow, about 20 - 40 mas wide. The velocity diagram in Fig. 9 shows that the [FeII] emission of the jet is blueshifted by -140 to -150 km s^{-1} relative to the systemic velocity of the molecular material around SVS 13 (Warin et al. 1996). A comparison of Figs. 7 and 9 demonstrates that the [FeII] emission is more blueshifted than the H_2 S(1) emission. The direct superposition of the H_2 and [FeII] emission line images shows that the bright portions of the microjet [FeII] emission extend up to the rim of the H_2 bubble, and that faint traces of [FeII] emission can be detected up to about the center of the bubble. The jet [FeII] intensity drops by a factor of ≈ 20 at the bubble surface. In fact, the brightest [FeII] along the jet axis is seen directly upwind from the H_2 bubble surface. The total 1.644 μm [FeII] flux is dominated by the emission outside of the expanding H_2 bubble. Since the front edge of the bright jet component near the bubble rim is not sharply defined, and subject to the degree of Lucy-Richardson deconvolution and the different quality of the adaptive optics correction achieved at the two epochs, we could not directly measure the proper motion of the jet front edge. From Fig. 3 it seems clear that the [FeII] shock emission from the jet is surrounded by an envelope of entrained ambient material radiating in the low-excitation shocked H_2 lines, and that at least the bright portions of the jet [FeII] emission terminate at the bubble rim. From the proper motion of the bubble front side, and the rate of bubble expansion (section 4.2), the expected, but not directly measured, proper motion of the side of the bubble facing SVS 13 (the back side in the direction of motion) is 6.6 mas yr^{-1}, which we also take as the proper motion of the front end of the bright jet. The length of the [FeII] jet is therefore changing only very slowly, at a rate of ≈ 7 mas $year^{-1}$, and the centroid of the [FeII] flux therefore moves at less than half this speed. This is responsible for the impression noted already by Davis et al. (2006) that the [FeII] emission looked stationary. What we see from the jet in the [FeII] emission line are either internal shocks or the shocks resulting from interaction with ambient molecular material that then gets entrained by the jet. The bulk of the jet material propagates into the area of the H_2 bubble, but the excitation conditions are, apparently, less favorable to the formation of such shocks radiating in [FeII].

We have tried, both on the 2012 and 2013 data, to detect the signature of jet rotation. Initially, using only the 2012 data, such rotation appeared to be indicated (Hodapp 2013). However, the 2013 data, and the re-reduced 2012 data with the new calibrations, did not confirm this (Fig. 9). The velocity pattern measured in 2013 was more confused and, if anything, a faint indication of the opposite rotation direction was found. In Fig. 9 (lower panels) we show the rms variations of the velocity measurements on the individual data

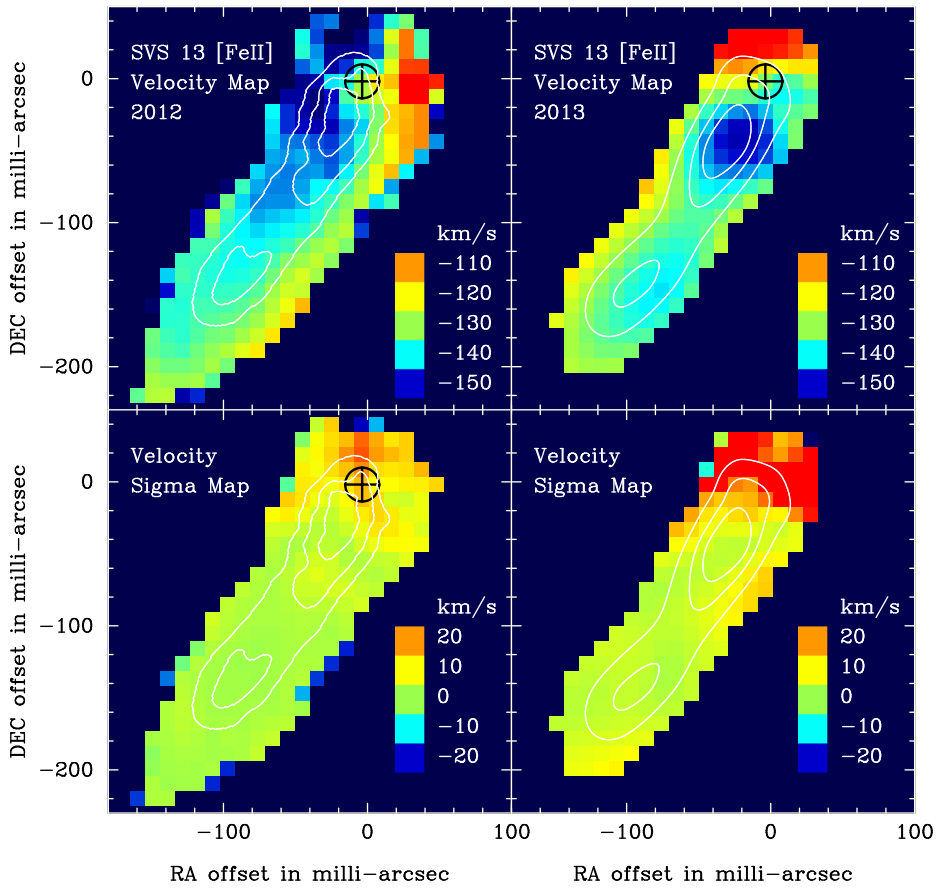

Fig. 9.— Top panels: Velocity map of the continuum-subtracted [FeII] 1.644 μm wavelength data cubes of the SVS 13 jet, deconvolved using the Lucy-Richardson algorithm, for the 2012 and 2013 data, respectively. The bottom panels show the corresponding velocity sigma maps. The white contours outline the line integrated [FeII] flux distribution. It clearly shows that all the line emission from the jet is blue-shifted relative to the systemic velocity of SVS 13. A color version of this figure is available in the electronic version of this paper.

cubes that were coadded to form the velocity maps in the top panels. These indicate that the errors of the velocity maps are below 10 km s^{-1} in most parts of the [FeII] jet. We conclude that the excellent spatial resolution and moderate spectral resolution of OSIRIS are not sufficient to resolve the kinematic signature of jet rotation in SVS 13.

4.6. Atomic Hydrogen Emission

The permitted atomic hydrogen line emission from SVS 13 was found to be broad with line widths of $\approx$ 180 $\pm$ 10 km s^{-1} for Brγ by Davis et al. (2001) and for Br-12 by Davis et al. (2003). The emission is centered on the position of the continuum source, but spatially unresolved. Our data cube in the Hn3 filter contains the Br-12 and Br-13 hydrogen recombination lines that trace the same hot hydrogen recombination regions as the more frequently used Br-γ does. In Fig. 10, we show the deconvolved images of SVS 13 across the Br-13 emission line after subtraction of the continuum emission. This figure confirms that emission in the atomic hydrogen recombination lines is spatially centered on the young star, and has the same flux profile as the continuum, i.e. we see no indication that the Br-13 emission is extended. Figure 10 has 10 mas pixels (2.35 AU), and any systematic differences between the line and continuum PSF are well below that angular scale. We conclude that the zone of atomic hydrogen emission, presumably the accretion disk itself, is less that 2 AU in extent. It is actually expected to be only of order of the dimensions of the star itself, i.e., about 2 orders of magnitude smaller than this limit. Our velocity data are consistent with the higher spectral resolution data of Davis et al. (2001) who found that the Brγ line is centered at -25 ($\pm$15) km s^{-1} relative to the systemic velocity of the SVS 13 core, essentially at the same velocity as the star.

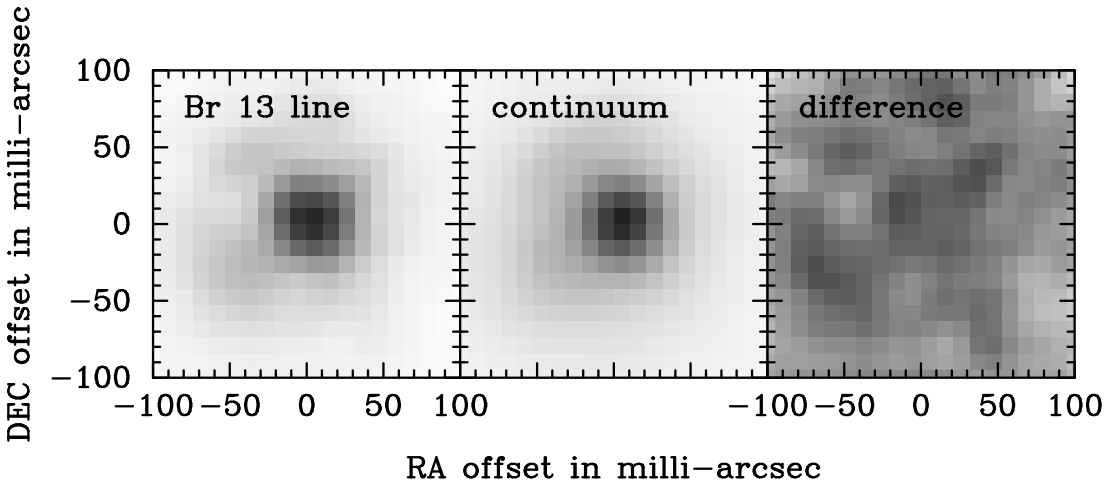

Fig. 10.— Left: Continuum-subtracted image of SVS 13 in the Br 13-4 line of atomic Hydrogen. Middle: Continuum adjacent to the line. Right: Ratio of these two, showing that the PSF is the same for the line emission and the continuum, within the limitations of the noise. This demonstrates that the H Br 13 line emission remains unresolved at the level of about 50 mas ($\approx$ 2 AU).

5. CONCLUSIONS

We have presented adaptive optics corrected integral field spectroscopy of the young outflow source SVS 13 in NGC 1333. The H_2 1–0 S(1) line at 2.122 μm, indicating low-velocity shocks, the higher excitation [FeII] line of the micro-jet at 1.644 μm, and atomic hydrogen emission in the HI12-4 and HI13-4 lines were analyzed and lead us to the following main conclusions:

1. The HH 7-11 outflow originates in SVS 13, which is identical to VLA 4B.
2. The outflow, at present, originates as a micro-jet of $\approx 0\farcs2$ length, detectable in [FeII] and oriented at P.A. 145°.
3. The formation of the youngest partly formed bubble visible in H_2 emission can be traced back to the $\approx$ 1990 outburst.
4. The bright parts of the [FeII] microjet reach up to the boundary of the H_2 S(1) bubble, but fainter [FeII] emission can be traced another $\approx 0\farcs2$ to near the center of the bubble.
5. Beyond that, H_2 S(1) emission outlines a curved path of the jet.
6. The orientation of the next two bubbles at P.A. $\approx$ 159° is roughly point-symmetric to the orientation of outflowing material in the counter-jet found by Bachiller et al. (2000) in CO and Raga et al. (2013) at 4.5 μm.
7. The chain of bubble fragments and their proper motions suggest that bubble-generating events are occurring repetitively, roughly every 30 years, at the present time.
8. The formation of a series of expanding bubbles within the outflow by a series of eruptive events provides an explanation for the widening of the outflow cavity.
9. Atomic hydrogen emission in the HI12-4 and HI13-4 (Brackett series) lines is detected around the continuum position of SVS 13, indicating ongoing accretion onto the star.
10. The outflow source SVS 13 remains at or near the peak brightness reached during the 1990 outburst. The light curve therefore resembles that of FUor type objects, while the emission line spectrum matches the characteristics of EXors. SVS 13 therefore represents an object somewhere between those classical classes.

Most of the data presented herein were obtained at the W.M. Keck Observatory, which is operated as a scientific partnership among the California Institute of Technology, the

University of California and NASA. The Observatory was made possible by the generous financial support of the W.M. Keck Foundation. Some photometric data on SVS 13 were obtained at the IRIS telescope on Cerro Armazones, which is operated under a cooperative agreement between the "Astronomisches Institut, Ruhr Universität Bochum", Germany, the "Universidad Catolica del Norte" in Antofagasta, Chile, and the Institute for Astronomy, University of Hawaii, USA. Construction of the IRIS infrared camera was supported by the National Science Foundation under grant AST07-04954. The operation of the IRIS telescope is supported by the "Nordrhein-Westfälische Akademie der Wissenschaften und der Künste" in the framework of the academy program by the Federal Republic of Germany and the state of Nordrhein-Westfalen. We wish to thank Angie Barr Dominguez, Thomas Dembsky, Holger Drass, Lena Kaderhandt, Michael Ramolla and Christian Westhues for operating the IRIS telescope for the acquisition of the data used in this paper, Ramon Watermann for writing the data reduction pipeline, and Roland Lemke for technical support. We thank Tuan Do and Jessica Lu for kindly providing the information about the OSIRIS spaxel scales on the Keck I and Keck II telescopes.

This publication makes use of data products from the Two Micron All Sky Survey, which is a joint project of the University of Massachusetts and the Infrared Processing and Analysis Center/ California Institute of Technology, funded by the National Aeronautics and Space Administration and the National Science Foundation. This publication also uses archival data obtained with the Spitzer Space Telescope, which is operated by the Jet Propulsion Laboratory, California Institute of Technology under a contract with NASA.

REFERENCES

Aldenius, M. & Johansson, S. 2007, A&A, 467, 753

Anglada,G. Rodríguez,L F. Osorio, M. José M. Torrelles, J. M. Estalella, R. Maria T. Belrtán, M. & Ho, P. T. P. 2004, ApJ, 605, L137

Anglada,G., Rodríguez, L F., & Torrelles, J., M. 2000, ApJ, 542, L123

Aspin, C., Reipurth, B., Herczeg, G. J., Capak, P. 2010, ApJ, 719, 50

Aspin, C., & Sandell, G. 1994, A&A, 288, 803

Bachiller, R., Gueth, F., Guilloteau, S., Tafalla, M., Dutrey, A. 2000, A&A, 362, L33

Bertin, E. 2005, in Astronomical Data Analysis Software and Systems XV, ASP Conference Series, Vol. 351, eds. Gabriel, C., Arviset, C, Ponz, D., & Solano, E., 112

Bertin, E. & Arnouts, S. 1996, A&AS, 117, 393

Bragg, S. L., Brault, J. W., & Smith, W. H. 1982, ApJ, 263, 999

Busso, M., Persi, P., Robberto, M., Scaltriti, F., Silvestro, G. 1987, in: Circumstellar Matter. IAU Symp. No. 122, eds. Appenzeller, I. and Jordan, C., Reidel, Dordrecht, p. 113

Camenzind, M. 1990, Reviews in Modern Astronomy, 3, 234

Carpenter, J. M. 2001, AJ, 121, 2851

Choi, M., Kang, M., & Tatematsu, K. 2011, ApJ, 728, L34

Chrysostomou, A., Hobson, J., Davis, C. J., Smith, M. D., & Berndsen, A. 2000, MNRAS, 314, 229

Codella, C., Cabrit, S., Gueth, F., et al. 2007, A&A, 462, L53

Cohen, M. & Schwartz, R. D. 1980, MNRAS, 191, 165

Cohen, M. & Schwartz, R. D. 1983, ApJ, 265, 877

Davis, C. J., Ray, T. P., Desroches, L., & Aspin, C. 2001, MNRAS, 326, 524

Davis, C. J., Stern, L., Ray, T. P., & Chrysostomou, A. 2002, A&A, 382, 1021

Davis, C. J., Whelan, E, Ray, T. P., & Chrysostomou, A. 2003, A&A, 397, 693

Davis, C. J., Nisini, B., Takami, M., Pyo, T.-S., Smith, M. D., Whelan, E., Ray, T. P., & Chrysostomou, A. 2006, ApJ, 639, 969

Davis, C. J., Cervantes, B., Nisini, B., Giannini, T., Takami, M., Whelan, E., Smith, M. D., Ray, T. P., Chrysostomou, A, & Pyo, T. S. 2011, A&A, 528, A3

Draine, B. T. 1980, ApJ, 241, 1021

Eislöffel, J., Günther, E., Hessman, F. V., Mundt, R., Poetzel, R., Carr, J. S., Beckwith, S., & Ray, T. P. 1991, ApJ, 383, L19

Fazio, G. G., Hora, J. L., Allen, L. E., et al. 2004, ApJS, 154, 10

Ferreira, J. 1997, A&A, 319, 340

Greene, T. P., Aspin, C., & Reipurth, B. 2008, AJ, 135, 1421

Harvey, P.M., Wiling, B. A., & Joy, M. 1984, ApJ, 278, 156

Herbig, G. H. 1977, ApJ, 217, 693

Herbig, G. H., Aspin, C., Gilmore, A. C., Imhoff, C. L., Jones, A. F. 2001, PASP, 113, 1547

Herbig, G. H., & Jones, B. F. 1983, AJ, 88, 1040

Hirota, T., Bushimata, T., Choi, Y. K. et al. 2008, PASJ, 60, 37

Hodapp, K. 2013, Protostars and Planets VI, 25

Hodapp, K. W., Bally, J., Eislöffel, J., & Davis, C. J. 2005, AJ, 129,1580

Hodapp, K. W., Chini, R., Reipurth, B., Murphy, M., Lemke, R., Watermann, R., Jacobson, S., Bischoff, K., Chonis, T., Dement, K., Terrien, R., & Provence, S. 2010, Proc. SPIE 7735-45.

Hodapp, K. W., Chini, R., Watermann, R., & Lemke, R. 2012, ApJ, 744, 56

Hodapp, K.-W., Hora, J. L., Hall, D. N. B., et al. 1996, New A, 1, 177

Hodapp, K.-W., Hora, J. L., Rayner, J. T., Pickles, A. J., & Ladd, E. F. 1996, ApJ, 468, 861

Hodapp, K. W., Iserlohe, C., Stecklum, B., & Krabbe, A. 2009, ApJ, 701, L100

Khanzadyan, T., Smith, M. D., Davis, C. J., Gredel, R., Stanke, T., & Chrysostomou, A. 2003, MNRAS, 338, 57

Königl, A., & Pudritz, R. F. 2000, Protostars and Planets IV, 759

Königl, A., & Pudritz, R. E. 2000, Protostars and Planets IV, 759

Kramida, A., Ralchenko, Yu., Reader, J., and the NIST ASD Team 2012, NIST Atomic Spectra Database (ver. 5.0), available at http://physics.nist.gov/asd

Krist, J. E., Stapelfeldt, K. R., Hester, J. J., Healy, K., Dwyer, S. J., & Gardner, C. L. 2008, AJ, 136, 1980

Larkin, J., Barczys, M., Krabbe, A., et al. 2006, Proc. SPIE, 6269, 42

Launhardt, R., Pavlyuchenkov, Y., Gueth, F., Chen, X., Dutrey, A., Guilloteau, S., Henning, Th., Piétu, V., Schreyer, K., & D. Semenov, D. 2009, A&A, 494, 147

Lee, C.-F., Hirano, N., Palau, A., et al. 2009, ApJ, 699, 1584

Liseau, R., Lorenzetti, D., & Molinari, S. 1992, A&A, 253, 119

Lucy, L. B. 1974, AJ, 79, 745

Mauron, N. & Thouvenot, E. 1991, IAU Circular 5261

Noriega-Crespo, A., Cotera, A., Young, E., & Chen, H. 2002, ApJ, 580, 959

Noriega-Crespo, A., & Garnavich, P. M. 2001, AJ, 122, 3317

Olofsson, H. 1980, private communication quoted by Liseau, Lorenzetti, & Molinari (1992)

Pech, G., Zapata, L. A., Loinard, L., & Rodríguez, L. F. 2012, ApJ, 751, 78

Raga, A. C., Noriega-Crespo, A., Carey, S. J., & Arce, H. G. 2013, AJ, 145, 28

Reipurth, B., & Bally, J. 2001, ARA&A, 39, 403

Richardson, W. H. 1972, J. Opt. Soc. Am. 62, 55

Rousselot, P., Lidman, D., Cuby, J.-G., Moreels, G., & Monnet, G. 2000, A&A, 354, 1134

Shu, F. H., Najita, J. R., Shang, H., & Li, Z.-Y. 2000, Protostars and Planets IV, 789

Skrutskie, M. F., Cutri, R. M., Stiening, R., Weinberg, M. D., Schneider, S., Carpenter, J. M., Beichman, C., Capps, R., Chester, T., Elias, J., Huchra, J., Liebert, J., Lonsdale, C., Monet, D. G., Price, S., Seitzer, P., Jarrett, T., Kirkpatrick, J. D., Gizis, J., Howard, E., Evans, T., Fowler, J., Fullmer, L., Hurt, R., Light, R., Kopan, E. L., Marsh, K. A., McCallon, H. L., Tam, R., Van Dyk, S., & Wheelock, S. 2006, AJ, 131, 1163

Strom, S. E., Vrba, F. J, & Strom, K. M. 1976, AJ, 81, 314

Takami, M., Chrysostomou, A., Ray, T. P., et al. 2006, ApJ, 641, 357

Tody, D. 1986, in Proc. SPIE, Instrumentation in Astronomy VI, ed. D. L. Crawford, 627, 733

Walawender, J., Bally, J., Francesco, J. D. Jrgensen, J. Getman, K. 2008 Handbook of Star Forming Regions, Volume I: The Northern Sky ASP Monograph Publications, Vol. 4. Edited by Bo Reipurth, p.346

Walsh, A. J., Myers, P. C., DiFrancesco, J., Mohanty, S., Bourke, T. L., Gutermuth, R., & Wilner, D. 2007, ApJ, 655, 958

Warin, S., Castets, A., Langer, W. D., Wilson, R. W., & Pagani, L. 1996, A&A, 306, 935

Zapata, L. A., Schmid-Burgk, J., Muders, D., et al. 2010, A&A, 510, A2

This preprint was prepared with the AAS LaTeX macros v5.2.